Structural and magnetic properties of amorphous Co_xZr_{100-x} films

Parul Rani●, Vladislav Kurichenko●, Emel Gürbüz●, Biplab Sanyal●, Björgvin Hjörvarsson●, and Gabriella Andersson●[*]

Department of Physics and Astronomy, Uppsala University, Box 516, SE-751 20 Uppsala, Sweden

Magnetometry and first-principles density functional theory-based calculations were used to investigate the concentration dependence of magnetic properties of amorphous Co_xZr_{100-x} alloys. A linear increase in saturation magnetization (M_s) is observed in both the experiments and calculations. Samples with Co content of at least 62 at.% are inferred to be ferromagnetic at 5 K. The experimentally determined ordering temperature is found to scale quadratically with Co concentration indicating a complex interplay between local structural motifs and magnetic parameters such as exchange interaction and anisotropy.

I. INTRODUCTION

The combination of two or more elements, forming alloys, is a classical route to control material properties. This is, e.g., exemplified in amorphous alloys, within which the absence of crystalline order, as well as control of other physical properties, can be obtained through the choice of composition [1,2]. Amorphous alloys lack long-range periodicity, however, hierarchical correlations can be observed at different length scales [3–5]. Variation in local composition results in changes in the atomic interactions, influencing the degree of short-to-medium range structural order, emerging during growth [6]. The distributions in coordination number and changes in the interatomic distances, therefore, pose a considerable challenge, since standard scattering techniques rely on the periodicity and are therefore of limited use [4,5,7]. However, electron, neutron, and x-ray scattering techniques are widely used to determine atomic pair distribution functions, providing a foundation for the development of structural models describing amorphous materials [4,5,8]. In recent years, significant progress has been made in the pursuit of detailed structural characterization of metallic glasses. For example, nanobeam electron diffraction [9] and atomic electron tomography [2] have been used to investigate local compositions as well as atomic configurations. The experimentally observed local orderings in amorphous materials can be reproduced through molecular dynamics simulations within good agreement [10]. Consequently, although amorphous alloys do not have a unique set of parameters defining the lack of atomic order, the use of statistical methods provides a good basis for comparing the results obtained in both experiments and modeling.

Amorphous Fe [11–14] and Co-based [15,16] magnetic alloys are widely investigated, as are the Co-early transition metals [17–20] and Co metalloids [21]. In many cases, an amorphous alloy has been used as a precursor for producing a magnetically soft nanocrystalline material for various applications [22,23]. The saturation magnetization M_s and magnetic ordering temperature T_c of amorphous Co-Zr-based alloys typically increase linearly with Co content, starting from zero at a critical concentration, which is usually in the range 40–60 at.% [6,22], in stark contrast to Fe-Zr alloys which show a nonlinear relation between composition and magnetic ordering temperature. Both M_s and T_c can be captured by atomistic models involving nearest-neighbor spin-spin interactions, which account for many of the defining characteristics of ferromagnetic ordering [6]. A question of interest is whether extrapolating the Co content to 100 at.% for this system gives magnetic properties which could be identified as those of pure amorphous Co. Furthermore, magnetic nanolaminates composed of alloy layers have been shown to exhibit large proximity effects arising at least partially from variation in composition at the nanoscale [24–26]. The composition variation at the nanoscale is argued to influence the material properties at that length scale, thereby causing a spatial dependence of, e.g., the magnetic moment, local magnetic anisotropy, and effective interactions. Here we present results from investigations of the influence of composition on the magnetic moment, ordering temperature and the effective interaction strength in amorphous Co_xZr_{100-x} thin films in the composition range $60 \leqslant x \leqslant 70$ at.%. The interpretation of the experimental observations is developed using calculations based on density functional theory, in an attempt to obtain an understanding of the impact of the local order and composition on macroscopic properties of amorphous alloys.

II. EXPERIMENTAL DETAILS

Co-Zr films of thickness 40 nm were deposited on Si(100) at room temperature by DC magnetron co-sputtering in an ultra-high-vacuum (UHV) chamber. The base pressure was $\sim 10^{-10}$ Torr and the sputtering gas (Argon) pressure was 2.0×10^{-3} Torr. The targets (three-inch diameter) were pure Co, Zr, and $Al_{70}Zr_{30}$. The Si(100) substrates were annealed in UHV conditions at 150 °C for 60 minutes to remove adsorbed

---

[*]gabriella.andersson@physics.uu.se

water and other surface impurities. During deposition, the substrate was rotated at 6 rpm for obtaining homogeneous growth. The Co content x was decreased from 70 at.% to 65 at.%, in steps of 1 at.% between subsequent samples, by the choice of Zr magnetron power, from 45 W to 57 W, while the Co magnetron power was fixed at 60 W. Beside these films, an additional sample with 60 at.% Co was deposited. Amorphous ~5 nm thick $Al_{70}Zr_{30}$ layers were used as seed and capping layers, preventing formation of nanocrystals at the interface to the substrate and oxidation of the surface, as described by Korelis *et al.* [11]. The procedure for cosputtering amorphous TM-Zr films has been described in detail previously [11,27,28].

Structural properties of the films were investigated using grazing incidence x-ray diffraction (GIXRD) and x-ray reflectivity (XRR) in a D-8 diffractometer with Cu K_α radiation (wavelength $\lambda = 0.15418$ nm). For the GIXRD measurements, the incident angle was fixed at $\omega = 1.0°$ and the detector angle was scanned through the range $2\theta = 10° - 80°$. XRR was recorded using θ–2θ scans up to $2\theta = 4.0°$. The composition was confirmed by Rutherford backscattering spectrometry (RBS).

Magnetization was measured in the temperature range 5–390 K using a Quantum Design MPMS XL superconducting quantum interference device (SQUID) magnetometer. The magnetic field was applied in-plane in all the measurements. In zero-field-cooled measurements, the samples were cooled from 300 K to 5 K in zero field. Once the sample temperature reached 5 K, a constant magnetic field of 2 mT was applied, and the total magnetic moment of the sample was recorded with increasing temperature. In field-cooled measurements, the total moment in a 2 mT applied field was recorded while decreasing the temperature. When measuring hysteresis loops at a constant temperature, the moment of the sample was recorded while varying the magnetic field. The magnetization of each sample was obtained by dividing the measured moment with the Co-Zr volume.

III. COMPUTATIONAL DETAILS

The local structure of the material was not measured directly, but could be reproduced through molecular dynamics simulations [10]. In our case, amorphous structures were generated by classical molecular dynamics (CMD) simulations with the open-source LAMMPS package [30] employing the embedded atom method (EAM) potential [31]. The total number of atoms ($N = 432$) in the cells was kept constant. We placed the Co and Zr atoms randomly in a cubic lattice using the experimental densities as a reference value. The amorphous structures were produced using the Berendsen thermostat [32] by the following procedure: Heating at 5000 K; fast quenching to 2000 K with a 51.28×10^{14} K/s cooling rate; applying short equilibration at 2000 K for 135 fs; quenching to 300 K with a 49.71×10^{13} K/s cooling rate and the final equilibrating step at 300 K for 3420 fs.

The quality of the metallic glass structure was checked by considering the $Co_{65}Zr_{35}$ alloy in first-principles molecular dynamics (FPMD) simulations based on the Born-Oppenheimer approximation, following the same thermostating steps with temperature rescaling at every 45 fs
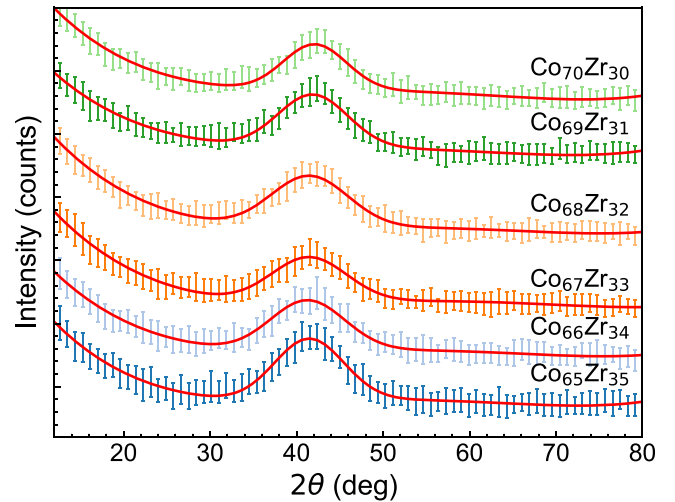

FIG. 1. Normalized GIXRD patterns, offset for clarity, of Co_xZr_{100-x} thin films with $65 \leqslant x \leqslant 70$ at.%, as indicated by the labels. The absence of sharp peaks indicates that the films are x-ray amorphous. The solid lines are Gaussian fits used to extract the center position of the broad feature at approximately $42°$. This hump is characteristic of a disordered material.

where the time step was set to 1 fs, using the Vienna *ab initio* simulation package (VASP) [33,34] within density functional theory (DFT). We employed the projector-augmented-wave (PAW) [35] formalism to describe the electron-ion interaction. The electron exchange and correlation (XC) potential was described by the Perdew-Burke-Ernzerhof (PBE) form within the generalized gradient approximation (GGA) [36]. For the Brillouin zone integration, we used the Γ point. The kinetic energy cut-off for the plane-wave basis set was 350 eV, and total energies were minimized with an energy tolerance of 10^{-4} eV. All atomic positions and lattice constants were optimized within the conjugate gradient method. We found a good agreement between the structures generated by CMD and FPMD simulations. To make a further stability test of our structures, we applied thermostating at 300 K by increasing the relaxation and simulation time in the following steps: 1 fs for 100 ps; 5 fs for 200 ps; 10 fs for 300 ps; and 1 ps for 1 ns.

IV. RESULTS AND DISCUSSION

A. Structural properties

Figure 1 shows the GIXRD measurements for the six Co_xZr_{100-x} films with $65 \leqslant x \leqslant 70$ at.%. No diffraction peaks are observed in the measurements which allows us to define the samples as x-ray amorphous [12,13]. A hump is observed at $2\theta \approx 42°$, and its width and position was fitted using a Gaussian model, also shown in Fig. 1. The centroid of the hump shifts toward higher angles with an increasing x, which can be understood as a decrease of interatomic distances with increasing Co content. The results from XRR measurements and the subsequent fits using *GenX* [29] are shown in Fig. 2. Fitting with a model including four layers was used to obtain interface roughness, thickness, as well as density of the $Al_{70}Zr_{30}$ and Co-Zr layers. A thin oxide layer is included in this model to account for the oxidation of the capping layer.
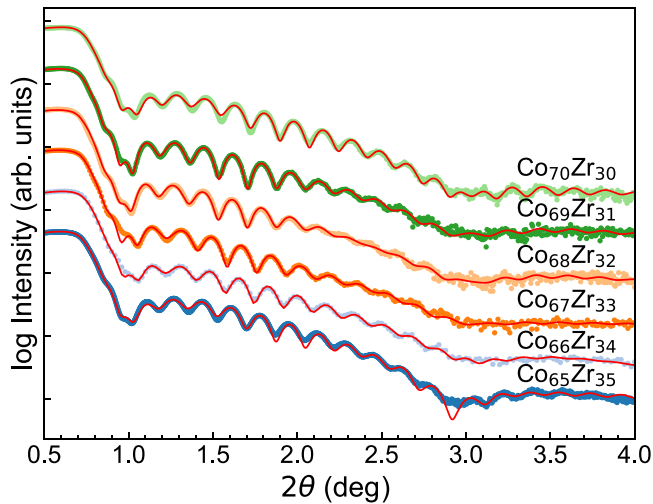
FIG. 2. XRR scans, offset for clarity, for the different 40 nm thick Co_xZr_{100-x} films with $65 \leqslant x \leqslant 70$ at.%. The solid red lines show the *GenX* [29] fits of the reflectivity data.

The results are consistent with well-defined layer thicknesses closely resembling the nominal values.

Analysis of the CMD simulated structures was done by studying the radial distribution function $g(r)$ (not shown) and Voronoi polyhedra. In $g(r)$ calculations, we used a 0.09 Å bin size. A shift in $g(r)$ toward smaller distances is observed with increasing Co content, in agreement with the GIXRD result. This shift also makes the double-peak character in $g(r)$ more visible, which is a fingerprint of Zr-based metallic glasses. These local structures do not have long-range translational symmetry but medium-range order (MRO). The most well-known SRO structures in Zr-based metallic glasses are icosahedra [37]. Specifically, these local structures exhibit a fivefold rotational symmetry and can be seen in two forms, perfect icosahedra ($\langle 0, 0, 12, 0 \rangle$) and distorted icosahedra ($\langle 0, 2, 8, 2 \rangle$; $\langle 0, 1, 10, 2 \rangle$; $\langle 0, 1, 10, 4 \rangle$; etc.). There are also fcc-types ($\langle 0, 2, 8, 4 \rangle$, etc.) and bcc-types ($\langle 0, 3, 6, 4 \rangle$, etc.) of SROs. The Voronoi indices for crystalline fcc/hcp and bcc are $\langle 0, 12, 0, 0 \rangle$ and $\langle 0, 6, 0, 8 \rangle$, respectively. Large variations are observed in the presence of different motifs at different Co concentrations, as seen in Fig. 3, where $x = 40$ at.% is deviating distinctly from $x = 65$ and $x = 70$ at.%. Hence, changes in the local configuration can considerably contribute to changes in the physical properties of the material. However, it should be noted that a systematic change in local structural motifs as a function of Co concentration may not be achieved clearly here, partially due to the magnetic degrees of freedom and partially due to the limited size ($N = 432$ atoms) of our samples used in simulations.

B. Magnetic properties

In-plane magnetization data, measured by SQUID magnetometry at $T = 5$ K, are shown in Fig. 4. The samples were first cooled to 5 K in zero field and thereafter $M(H)$ loops were recorded. Smaller steps were used in the low-field region, shown in the figure inset, in order to accurately measure the coercivity, H_c, of the samples. For $x = 65$ at.%, the coercivity and the saturation magnetization are $\mu_0 H_c = 4.7$ mT
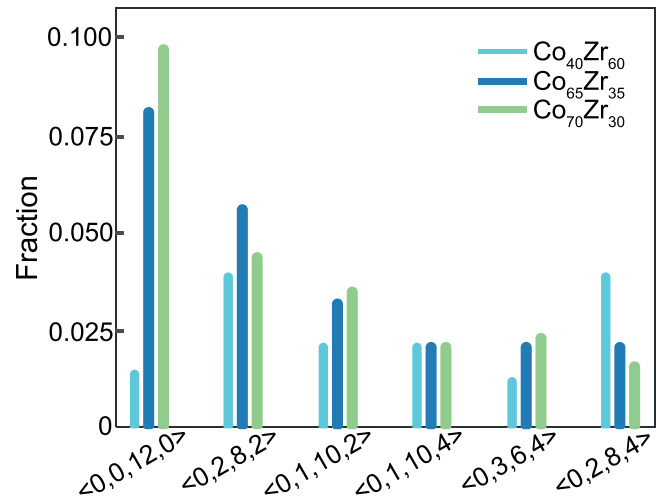

FIG. 3. Analysis of Voronoi polyhedra of selected compositions from the structures obtained from CMD simulations.

and $M_s = 0.24 \mu_B$/Co atom, respectively. The loop shapes reveal that all these samples are ferromagnetic, and all Co moments are fully aligned well below the maximum applied field (500 mT). Magnetization measurements at 5 K on the $Co_{60}Zr_{40}$ film showed no detectable ferromagnetic response.

Figure 5 shows both the experimental (SQUID) and the calculated (DFT) saturation magnetization, M_s, versus Co content, x. The difference between theory and experiment may come from the choice of exchange and correlation functional in DFT and/or the limited size of the simulated structures. However, in both data sets, M_s increases linearly with x in the investigated composition range. When the linear dependence is extrapolated to pure Co ($x = 100$ at.%), the effective moment per Co atom is $2.5 \mu_B$ from experiments and $2.0 \mu_B$ from the DFT calculations. These values are higher than the hcp Co moment ($1.55 \mu_B$) [38]. The linear fit of the experimental data crosses $M_s = 0$ for $x = 61.5$ at.% ($x = 50.6$ at.% for calculated M_s), which is in agreement with the experimental result that the $x = 60$ at.% sample is nonmagnetic at $T = 5$ K.
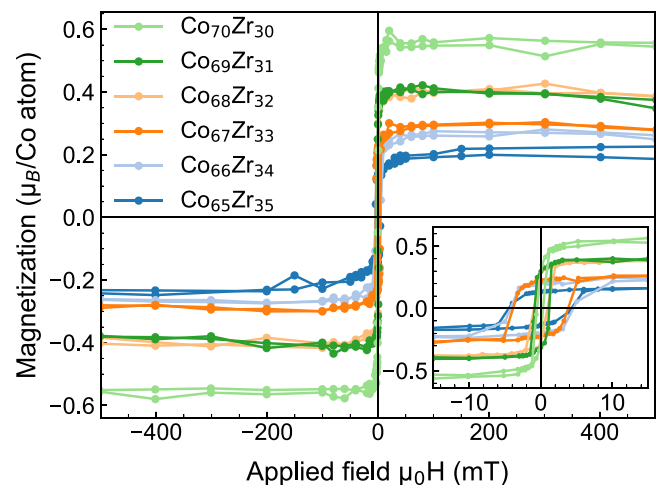

FIG. 4. In-plane hysteresis loops measured at 5 K for amorphous Co_xZr_{100-x} thin films. Inset: Magnified low-field region, showing the coercivities of all samples.
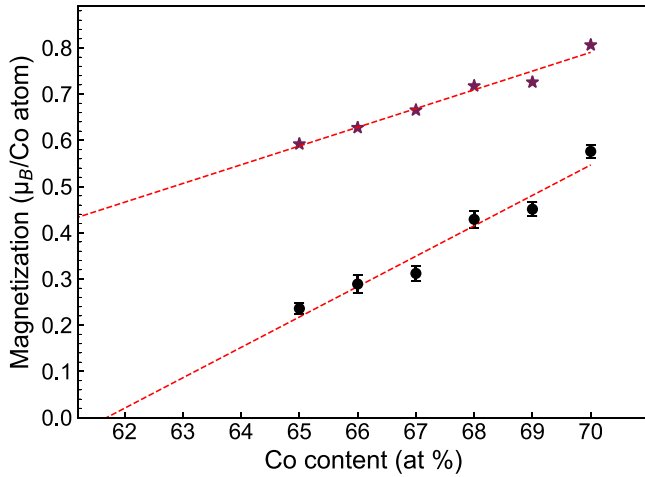
FIG. 5. Saturation magnetization, displayed as moment per Co atom versus Co content. Stars (calculated by DFT, $T = 0$ K) and circles (measured by SQUID, $T = 5$ K) are the data points, and the dashed red lines show linear fits.

The coercivity of the samples is observed to increase with increasing Zr content. This could be caused by an increase in spin orbit coupling or, more likely, a decrease in magnetic leverage [39] with decreasing Co moments.

In order to determine changes in the ordering temperature (T_c), we measured the temperature dependence of the magnetization in an applied magnetic field of 2 mT. The choice of nonzero field conditions was motivated by the minimization of random errors associated to measurements in zero field. Prior to the measurements, the samples were cooled in the absence of field. The results are displayed in Fig. 6. For estimating T_c, the $M(T)$ data were fitted by minimizing the expression [14]

$$\xi^2 = \frac{1}{n-2} \sum_{i_{t \min}}^{i_{t \max}} \left[\log_{10} M_i - \left[\log_{10} k + \beta \log_{10} \left(1 - \frac{T}{T_c} \right) \right] \right]^2. \tag{1}$$

Here n is the number of data points included in the fit, $t = T/T_c$ is the reduced temperature, $t_{\max}$ and $t_{\min}$ are

maximum and minimum t values included, M is the normalized magnetization, k is a constant, and β is an effective exponent. In this context, β is not considered a critical exponent, since amorphous alloy systems have random atomic distributions and therefore composition inhomogeneities at the nanometer scale [2]. The minimization of ξ^2 in Eq. (1) was performed with the Broyden-Fletcher-Goldfarb-Shanno (BFGS) algorithm [40]. The experimental $M(T)$ data and fitting results of M versus t are shown in Fig. 6(a). For the $x = 65$ at.% sample, $T_c \approx 39.5$ K is observed. All $M(T)$ curves have a similar shape, and T_c increases with increasing Co content x, as shown in Fig. 6(b). The magnetization just above T_c exhibits significant tailing. The tail arises partially from the applied field (2 mT), while significant contributions can be argued to originate from inhomogeneities in the random Co concentration distribution, as discussed in Refs. [2,6,14]. The tailing becomes more apparent when plotting the changes in magnetization using normalized temperatures, as seen in the inset in Fig. 6(a). The precision of the determined Curie temperatures is substantially better than the accuracy of the measurements. The increase in T_c with x [Fig. 6(b)] appears to include a quadratic term, which opens up for questions concerning the role of coordination numbers for the effective interaction in the alloy. More detailed investigations are required for answering these questions, for example comparing the changes in the Curie temperature and moment in a wider concentration span.

V. CONCLUSIONS

The experimentally and theoretically determined saturation moments of Co_xZr_{100-x} alloys are found to scale linearly with the Co concentration, in the concentration range explored ($65 \leqslant x \leqslant 70$ at.%). In contrast to this, the experimentally determined ordering temperature is found to increase quadratically with Co concentration within this range. Assuming the ordering temperature to scale with the effective coupling, we have an indication of an increase in the effective coupling with increasing Co concentration in Co_xZr_{100-x} alloys. The coordination numbers of Co atoms are inferred to change
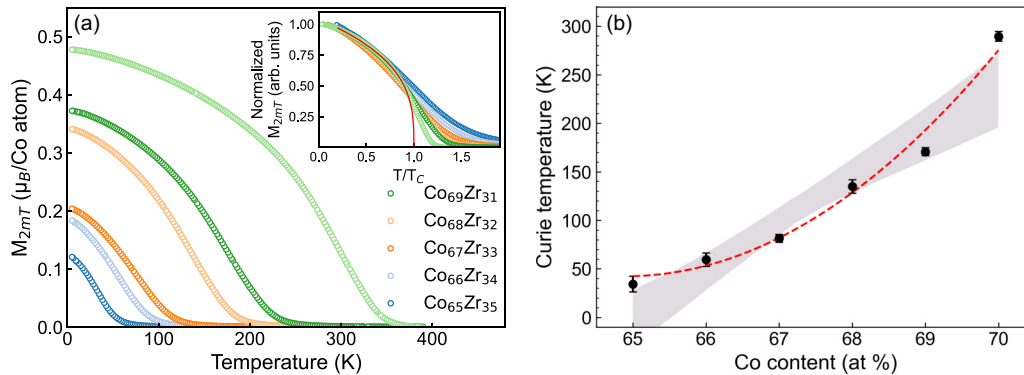

FIG. 6. (a) Raw data from all samples, $65 \leqslant x \leqslant 70$ at.%, of field-cooled magnetization versus temperature at 2 mT. The inset shows the normalized magnetization as a function of the reduced temperature $t = T/T_c$ together with the fits (solid red lines) to Eq. (1). The accuracy in the determination of the ordering temperature is affected by the tailing. (b) The Curie temperature as a function of Co content, with a quadratic fit (dashed line). The precision in the determination of the Curie temperature is provided as error bars. The shaded area marks the uncertainty range when performing linear fit.

with concentration using Voronoi polyhedra analysis of the simulated structures. We therefore have a correlation of the nontrivial changes in the effective coupling and the effective coordination number of Co with composition. However, it is not possible to relate these observations in a causal manner. More investigations are required to explore these nontrivial effects, linking the structural changes in disordered materials with variations in, e.g., magnetic exchange coupling with concentration.

[1] A. L. Greer, Metallic glasses, Science **267**, 1947 (1995).

[2] R. Gemma, A. Pundt, V. Kapaklis, and B. Hjörvarsson, The impact of nanoscale compositional variation on the properties of amorphous alloys, Sci. Rep. **10**, 11410 (2020).

[3] Y. Hiraoka, T. Nakamura, A. Hirata, E. G. Escolar, K. Matsue, and Y. Nishiura, Hierarchical structures of amorphous solids characterized by persistent homology, Proc. Natl. Acad. Sci. **113**, 7035 (2016).

[4] H. Sheng, W. Luo, F. Alamgir, J. Bai, and E. Ma, Atomic packing and short-to-medium-range order in metallic glasses, Nature (London) **439**, 419 (2006).

[5] D. Ma, A. D. Stoica, and X.-L. Wang, Power-law scaling and fractal nature of medium-range order in metallic glasses, Nat. Mater. **8**, 30 (2009).

[6] K.A. Thórarinsdóttir, N. Strandqvist, V. Sigurjónsdóttir, E. Thorsteinsson, B. Hjörvarsson, and F. Magnus, Finding order in disorder: Magnetic coupling distributions and competing anisotropies in an amorphous metal alloy, APL Mater. **10**, 041103 (2022).

[7] S. George, K. Kádas, P. E. Jönsson, G. Muscas, F. Magnus, O. Eriksson, A. Delin, and G. Andersson, Local structure in amorphous Sm_xCo_{1-x} a combined experimental and theoretical study, J. Mater. Sci. **55**, 12488 (2020).

[8] C. Benmore, A review of high-energy x-ray diffraction from glasses and liquids, International Scholarly Research Notices **2012**, 852905 (2012).

[9] A. Hirata, P. Guan, T. Fujita, Y. Hirotsu, A. Inoue, A. R. Yavari, T. Sakurai, and M. Chen, Direct observation of local atomic order in a metallic glass, Nat. Mater. **10**, 28 (2011).

[10] A. Hirata, L. Kang, B. Klumov, K. Matsue, M. Kotani, A. Yavari, and M. Chen, Geometric frustration of icosahedron in metallic glasses, Science **341**, 376 (2013).

[11] P. T. Korelis, A. Liebig, M. Björck, B. Hjörvarsson, H. Lidbaum, K. Leifer, and A. Wildes, Highly amorphous $Fe_{90}Zr_{10}$ thin films, and the influence of crystallites on the magnetism, Thin Solid Films **519**, 404 (2010).

[12] P.T. Korelis, P. E. Jönsson, A. Liebig, H.-E. Wannberg, P. Nordblad, and B. Hjörvarsson, Finite-size effects in amorphous $Fe_{90}Zr_{10}/Al_{75}Zr_{25}$ multilayers, Phys. Rev. B **85**, 214430 (2012).

[13] P. Sharma, H. Kimura, and A. Inoue, Magnetic behavior of cosputtered Fe-Zr amorphous thin films exhibiting perpendicular magnetic anisotropy, Phys. Rev. B **78**, 134414 (2008).

[14] M. Ahlberg, P. T. Korelis, G. Andersson, and B. Hjörvarsson, Effect of ferromagnetic proximity on critical behavior, Phys. Rev. B **85**, 224425 (2012).

[15] G. Suran, M. Naili, and J. Sztern, Induced magnetic anisotropy related to the local atomic order: A study in amorphous Co-Zr and Co-Zr-M thin films, J. Appl. Phys. **63**, 4318 (1988).

[16] G. Suran, M. Naili, H. Niedoba, F. Machizaud, O. Acher, and D. Pain, Magnetic and structural properties of Co-rich CoFeZr amorphous thin films, J. Magn. Magn. Mater. **192**, 443 (1999).

[17] N. Heiman and N. Kazama, Concentration dependence of the Co moment in amorphous alloys of Co with Y, La, and Zr, Phys. Rev. B **17**, 2215 (1978).

[18] Y. Shimada and H. Kojima, Sputtering of amorphous Co-Zr and Co-Hf films with soft magnetic properties, J. Appl. Phys. **53**, 3156 (1982).

[19] Y. Kakehashi, M. Yu, and H. Tanaka, Enhancement of Curie temperature in amorphous Co-Y alloys, Materials Science and Engineering: A **181-182**, 946 (1994).

[20] M. Ali and P. Grundy, Magnetic properties of crystalline and amorphous Co-Zr, Nb, Mo thin film alloys, J. Phys. D **16**, 2239 (1983).

[21] H. Tanaka, S. Takayama, M. Hasegawa, T. Fukunaga, U. Mizutani, A. Fujita, and K. Fukamichi, Electronic structure and magnetism of amorphous $Co_{1-x}B_x$ alloys, Phys. Rev. B **47**, 2671 (1993).

[22] X. F. Yao, J. P. Wang, T. J. Zhou, and T. C. Chong, Microstructure and magnetic properties of CoZr thin film, J. Appl. Phys. **93**, 8310 (2003).

[23] F. Li, T. Liu, J. Zhang, S. Shuang, Q. Wang, A. Wang, J. Wang, and Y. Yang, Amorphous–nanocrystalline alloys: Fabrication, properties, and applications, Materials Today Advances **4**, 100027 (2019).

[24] H. Palonen, B. Mukhamedov, A. Ponomareva, G. K. Pálsson, I. Abrikosov, and B. Hjörvarsson, The magnetization profile induced by the double magnetic proximity effect in an $Fe/Fe_{0.30}V_{0.70}$ superlattice, Appl. Phys. Lett. **115**, 012406 (2019).

[25] F. Magnus, M. Brooks-Bartlett, R. Moubah, R. Procter, G. Andersson, T. Hase, S. Banks, and B. Hjörvarsson, Long-range

magnetic interactions and proximity effects in an amorphous exchange-spring magnet, Nat. Commun. **7**, 11931 (2016).

[26] K.A. Thórarinsdóttir, H. Palonen, G. Palsson, B. Hjörvarsson, and F. Magnus, Giant magnetic proximity effect in amorphous layered magnets, Phys. Rev. Mater. **3**, 054409 (2019).

[27] H. Raanaei, H. Nguyen, G. Andersson, H. Lidbaum, P. Korelis, K. Leifer, and B. Hjörvarsson, Imprinting layer specific magnetic anisotropies in amorphous multilayers, J. Appl. Phys. **106**, 023918 (2009).

[28] A. Frisk, M. Ahlberg, G. Muscas, S. George, R. Johansson, W. Klysubun, P. E. Jönsson, and G. Andersson, Magnetic and structural characterization of CoFeZr thin films grown by combinatorial sputtering, Phys. Rev. Mater. **3**, 074403 (2019).

[29] M. Björck and G. Andersson, *GenX*: An extensible X-ray reflectivity refinement program utilizing differential evolution, J. Appl. Crystallogr. **40**, 1174 (2007).

[30] S. Plimpton, Fast parallel algorithms for short-range molecular dynamics, J. Comput. Phys. **117**, 1 (1995).

[31] J. Cai and Y.Y. Ye, Simple analytical embedded-atom-potential model including a long-range force for fcc metals and their alloys, Phys. Rev. B **54**, 8398 (1996).

[32] H. J. Berendsen, J. v. Postma, W. F. Van Gunsteren, A. DiNola, and J. R. Haak, Molecular dynamics with coupling to an external bath, J. Chem. Phys. **81**, 3684 (1984).

[33] G. Kresse and J. Hafner, Ab initio molecular dynamics for liquid metals, Phys. Rev. B **47**, 558 (1993).

[34] G. Kresse and J. Furthmüller, Efficient iterative schemes for ab initio total-energy calculations using a plane-wave basis set, Phys. Rev. B **54**, 11169 (1996).

[35] P. E. Blöchl, Projector augmented-wave method, Phys. Rev. B **50**, 17953 (1994).

[36] J. P. Perdew, K. Burke, and M. Ernzerhof, Generalized gradient approximation made simple, Phys. Rev. Lett. **77**, 3865 (1996).

[37] Y. Q. Cheng, H. W. Sheng, and E. Ma, Relationship between structure, dynamics, and mechanical properties in metallic glass-forming alloys, Phys. Rev. B **78**, 014207 (2008).

[38] C. Li, A. Freeman, and C. Fu, Electronic structure and magnetic properties of the hcp Co (0001) surface, J. Magn. Magn. Mater. **94**, 134 (1991).

[39] R. A. Procter, F. Magnus, G. Andersson, C. Sánchez-Hanke, B. Hjörvarsson, and T. P. A. Hase, Magnetic leverage effects in amorphous SmCo/CoAlZr heterostructures, Appl. Phys. Lett. **107**, 062403 (2015).

[40] R. Fletcher, *Practical Methods of Optimization* (John Wiley & Sons, Hoboken, New Jersey, 2013).